Supporting Information for

# Integration of chemical component control and a pillared parallel structure for efficient water electrolysis

Chengjie Wu,[a] Xuesong Liu,[a] Kuan Deng,[a] Wen Tian,[a,] * Junyi Ji[a, b,] *

[a] School of Chemical Engineering, Sichuan University, Chengdu 610065, P. R. China

[b] State Key Laboratory of Polymer Materials Engineering, Sichuan University, Chengdu 610065, P. R. China

* Corresponding author. E-mail address

Junyi Ji, E-mail: junyiji@scu.edu.cn

Wen Tian, E-mail: tianwen591@scu.edu.cn

## S1 Chemicals and materials

Dopamine hydrochloride (DA-HCl, AR 98%), tris(hydroxymethyl) aminomethane (Tris, AR 99%), hexamethylenetetramine (HMT, AR 99%), potassium hexacyanoferrate ($K_3[Fe(CN)_6]$, AR 99%), potassium hexacyanocobaltate ($K_3[Co(CN)_6]$, AR 99%) and potassium hydroxide (KOH, AR 95%) were purchased from Aladdin. Nickle nitrate hexahydrate ($Ni(NO_3)\cdot 6H_2O$, AR 98%), ($H_2NCONH_2$, AR), ammonium fluoride ($NH_4F$, AR), anhydrous ethanol, and hydrochloric acid (HCl, AR 35-37%) were purchased from Chengdu Chron Chemicals Co., Ltd. Nickel foam (NF, 99.8%) was purchased from Chengdu Taiyu Gas Co., Ltd. The commercial $IrO_2$/Ti electrodes was purchased from Kunshan Yiwanlin Electronic Technology Co., Ltd. for electrochemical tests. All chemical reagents in the experiment were utilized directly without purification.

## S2 Fabrication of the composites

### Synthesis of $Ni(OH)_2$/NF-D

First, Ni Foam (NF) was treated with ethanol, hydrochloric acid (1 M), and deionized (DI) water to remove the surface oxides and organic molecules. Then, $Ni(OH)_2$ nanosheet arrays with disordered alignment ($Ni(OH)_2$/NF-D) was prepared by hydrothermal method. $Ni(NO_3)_2 \cdot H_2O$ (2.9 g), hexamethylenetetramine (HMT) (2.8 g) were dissolved into 70 mL of DI water under magnetic stirring. Subsequently, the NF and aqueous $Ni(NO_3)_2$/HMT solution were transferred to a Teflon-lined stainless-steel autoclave and heated at 100 °C for 4 h. After naturally cooling to ambient temperature, the products were cleaned with ethanol and deionized water, and dried at 60 °C for 6 h.

### Synthesis of NiO-FeO/NF-P, NiO-CoO/NF-P and $Ni_2P$/NF-P

The as-prepared NiFe PBA/NF-P or NiCo PBA/NF-P samples were placed in a tubular furnace and subjected to thermal treatment under a continuous flow of high-purity argon gas (50 sccm). The temperature was ramped from room temperature to 350 °C at a rate of 2 °C $min^{-1}$, followed by annealing at 350 °C for 3 h. After the heat treatment, the furnace was allowed to cool naturally to room temperature. The resulting products were denoted as NiO-FeO/NF-P and NiO-CoO/NF-P, respectively.

### Synthesis of $Ni_2P$/NF-P

The obtained $Ni(OH)_2$/NF-P sample was placed at the downstream end of a tubular furnace, while 100 mg of $NaH_2PO_2 \cdot H_2O$ was positioned at the upstream end, with a separation distance of approximately 5 cm between the two. The phosphorization was conducted under a continuous flow of high-purity argon gas (50 sccm). The temperature was increased from room temperature to 350 °C at a heating rate of 2 °C $min^{-1}$ and maintained at 350 °C for 3 h. After the reaction, the furnace was allowed to cool naturally to room temperature. The resulting product was denoted as $Ni_2P$/NF-P.

## S3 Materials Characterization

The morphology and microstructure of the catalysts were characterized by scanning electron microscope (SEM, JEOL JSM 7610F), energy dispersive X-ray spectroscopy (EDS), and transmission electron microscopy (TEM, FEI Tecnai G20). The crystalline structures and chemical valence states were identified by X-ray diffraction (XRD, Cu Kα radiation, Rigaku, SmartLab) and X-ray photoelectron spectroscopy (XPS, PHI5000 Versa spectrometer). The Raman was performed on a confocal Raman spectrometer (Renishaw, InVia Qontor) using an excitation of 532 nm laser.

**S4 Electrochemical measurement**

Electrochemical measurements were performed with a CHI 760E electrochemical workstation (CH Instruments, Inc.) at room temperature unless stated otherwise. A three-electrode configuration was employed, including a working electrode (the prepared materials), reference electrode (saturated Hg/HgO), and a counter electrode (graphite rod). The electrochemical characterizations were conducted in an electrolyte of 1 M KOH (pH = 14). The relevant RHE potential was calculated following the Nernst equation: $E_{RHE} = E_{Hg/HgO} + 0.059 \times pH + 0.098$ V. All electrochemical curves were recorded after activating the catalysts with cyclic voltammetry (CV) at a scan rate of 50 $mV \cdot s^{-1}$ (0.924 –1.624 V vs. RHE for OER and UOR) until a stable state was reached.

To observe the change of redox peak in the process of polarization, OER and UOR activity was assessed by CV at a scan rate of 2 $mV \cdot s^{-1}$ with iR correction. The overpotential (η) for OER was calculated by $\eta_{OER} = E_{RHE} - 1.23$ V, while $E_{RHE}$ was obtained from the cathode polarization curve. The correction is carried out in accordance with $E=E_{RHE}$-IR, where I is the corresponding current and R is the solution resistance obtained in the EIS figure.

The Tafel plots were obtained by plotting as overpotential (η) versus the logarithm of current density (log *j*) based on polarization curves.

The Tafel slope is obtained by fitting the LSV (CV) curve as $\eta = a + b \cdot \log j$, η is the reversible hydrogen electrode potential, j is the current density, and b is the Tafel slope.

Electrochemical impedance spectroscopy (EIS) was tested from 0.1 Hz to 100 kHz at an overpotential of 330 mV (vs. RHE) for OER and UOR.

Assessment of turnover frequency (TOF): TOF ($s^{-1}$) was calculated as follows:

$$TOF = \frac{I}{\alpha F n}$$

While I is the corresponding current (A) at a specific voltage in the LSV curve, α is the number of electrons transferred by the half-reaction (OER: α = 4), F is the Faraday constant (96485 C $mol^{-1}$), n is the number of active sites.

The number of active sites was determined by the CV curves recorded between –

0.2 and 0.6 V (vs. RHE) in PBS buffer solution (pH = 7.4) at a scan rate of 50 $mV \cdot s^{-1}$. The number of active sites (n) was calculated at non-Faradaic regions according to the following equation:

$$n = \frac{Q}{\alpha F}$$

Where Q is the amount of charge transferred during the CV test.

The electrochemical active area (ECSA) was calculated according to following equation:

$$ECSA = \frac{C_{dl}}{C_s}$$

$C_s$ is the specific capacitance in an alkaline electrolyte and $C_{dl}$ is obtained from the cyclic voltammetry within the non-Faradaic region at different scan rates. $C_s$ = 0.04 $mF \cdot cm^{-2}$.[1] The $C_{dl}$ value equals the slope of the linear relationship between the scan rate and current density. The measured sweep speed was 10-100 $mV \cdot s^{-1}$ and the CV measurement voltage windows were 0.924 - 1.024 (vs. RHE) for OER and UOR:

The stability was tested by the chronoamperometry method (i - t).

## Supporting Figures

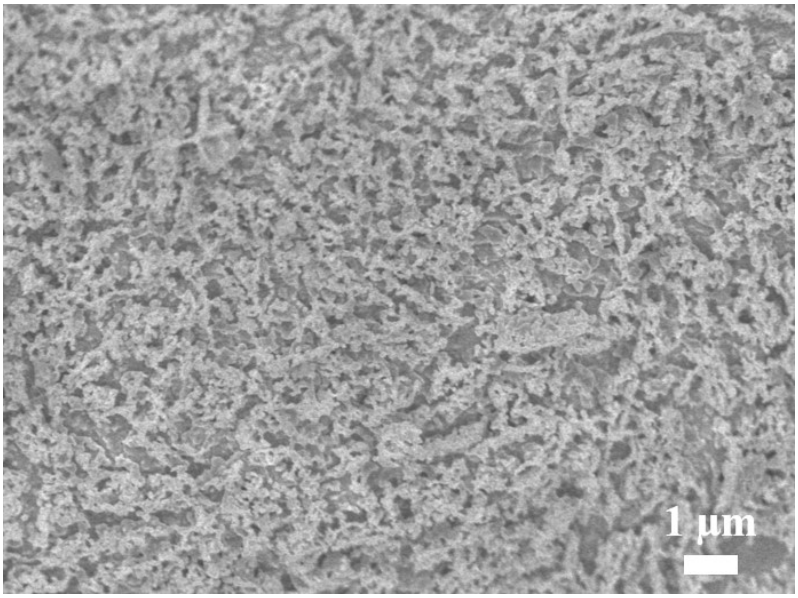


**Fig. S1.** SEM image of $Ni_2P$/NF-P.

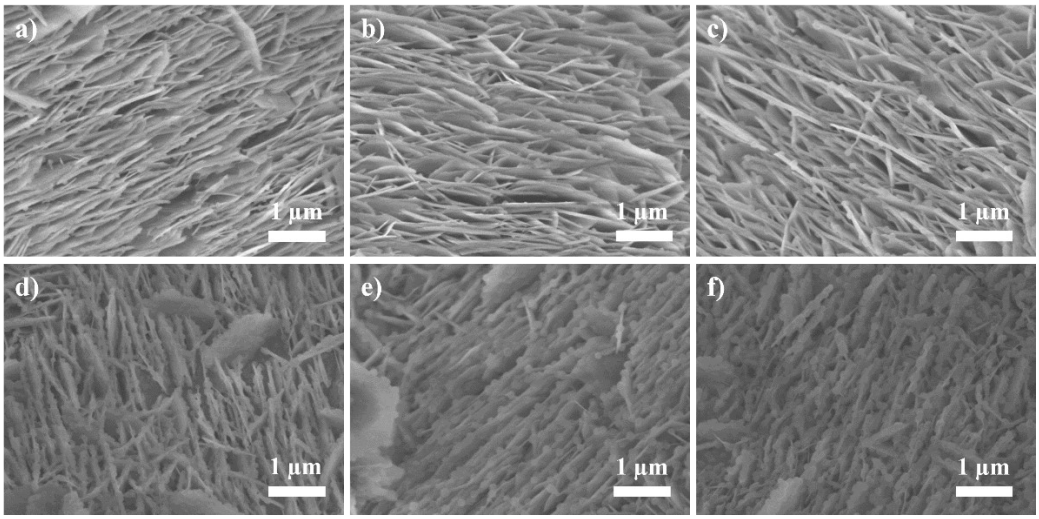


**Fig. S2.** SEM images of $Ni(OH)_2$/NF-P soaked in $K_3[Fe(CN)_6]$ solution for different time periods: (a) 4 h, (b) 8 h, (c) 12 h, (d) 16 h, (e) 20 h, (f) 24 h.

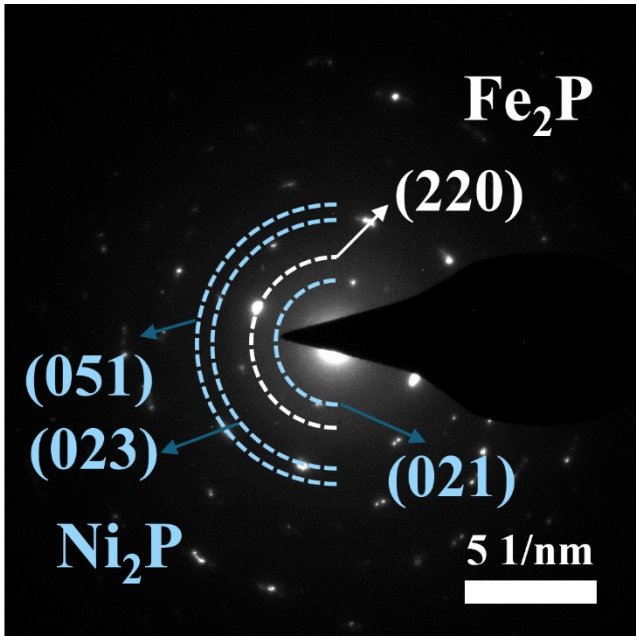


**Fig. S3.** SAED pattern of the $Ni_2P$-$Fe_2P$/NF-P.

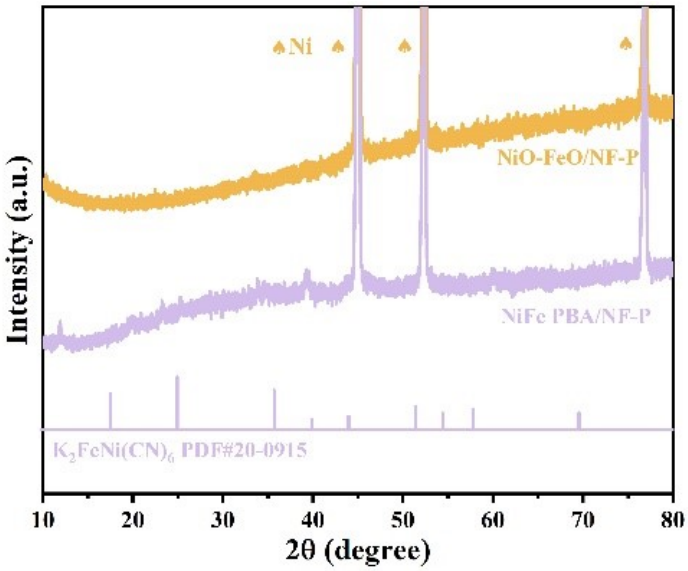


**Fig. S4.** XRD patterns of the NiFe PBA/NF-P and NiO-FeO/NF-P.

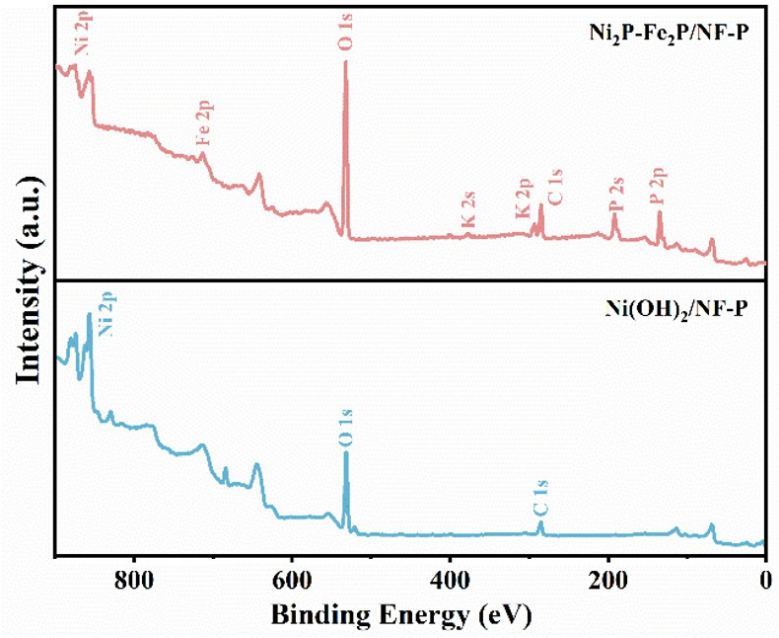


**Fig. S5.** The XPS full survey of $Ni_2P$-$Fe_2P$/NF-P and $Ni(OH)_2$/NF-P.

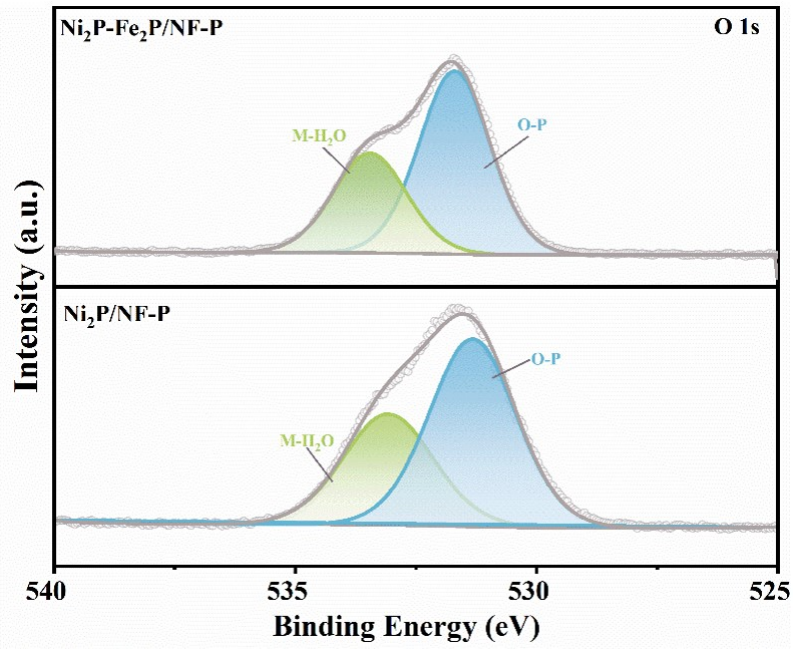


**Fig. S6.** The XPS spectrum of O 1s.

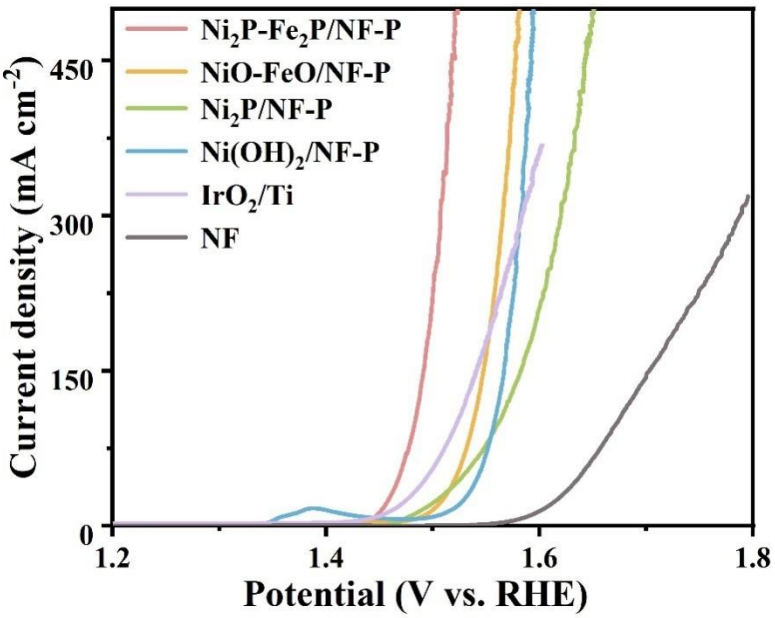


**Fig. S7.** Reverse scan LSV curves with iR compensation.

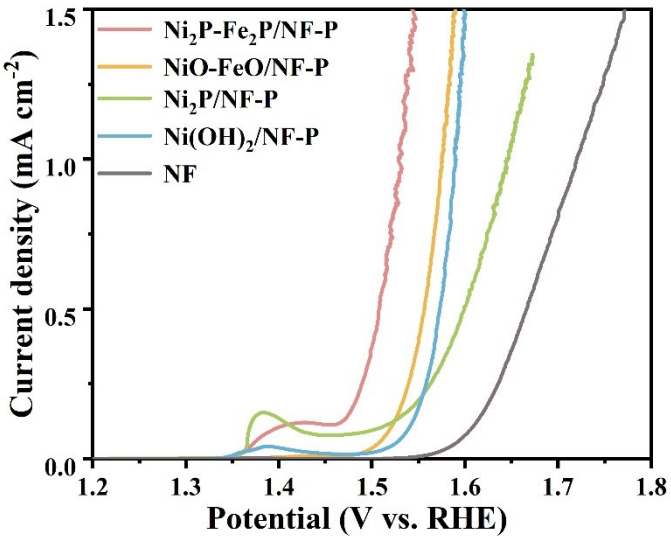


**Fig. S8.** ECSA-normalized LSV curves for OER corresponding to **Fig. 3a**.

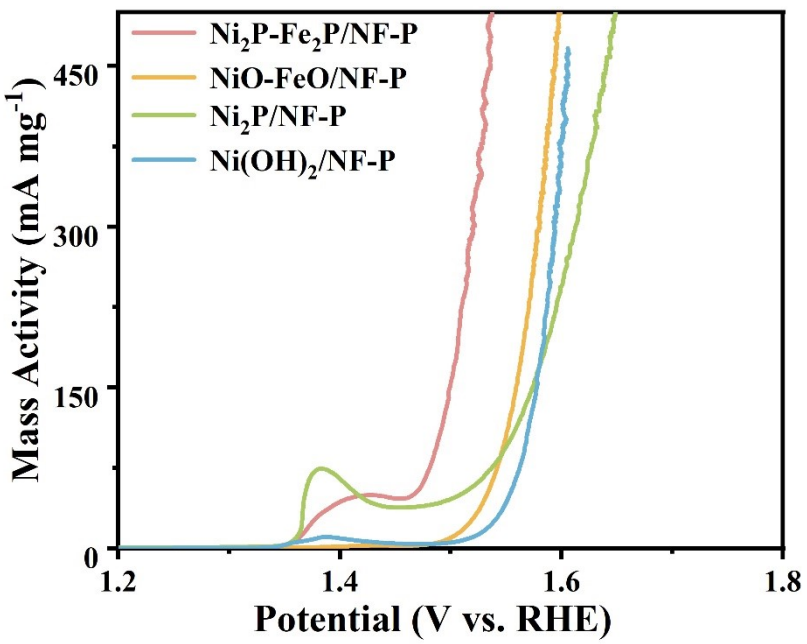


**Fig. S9.** Active material loading mass-normalized LSV curves for OER corresponding to **Fig. 3a**.

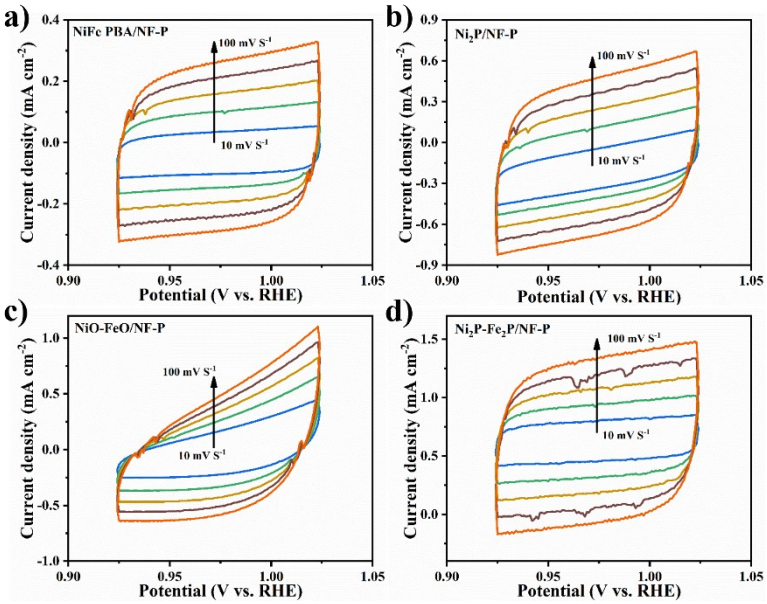


**Fig. S10.** CV curves of (a) NiFe PBANF-P, (b) $Ni_2P$/NF-P, (c) NiO-FeO/NF-P, (d) $Ni_2P$-$Fe_2P$/NF-P.

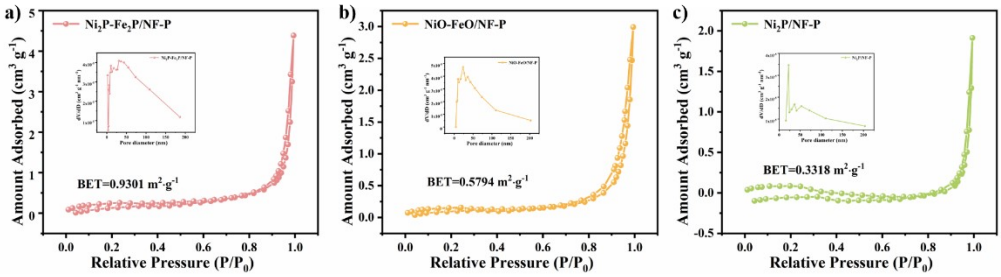


**Fig. S11.** Adsorption-desorption isotherms and pore size distribution (inset) of the $Ni_2P$-$Fe_2P$/NF-P, NiO-FeO/NF-P and $Ni_2P$/NF-P.

The BET measurement for the as-prepared composites was also investigated. As the active materials are anchored on the nickel foam surface, the calculated specific surface area remains within relatively low values. Typically, the $Ni_2P$-$Fe_2P$/NF-P exhibits a higher BET surface area (0.93 $m^2$ $g^{-1}$) than the control samples (0.33 $m^2$ $g^{-1}$ for $Ni_2P$/NF-P and 0.58 $m^2$ $g^{-1}$ for NiO-FeO/NF-P). When considering the various loading mass and the NF substrate (1.61, 1.58, 1.03 and 38.23 mg $cm^{-2}$ for $Ni_2P$-$Fe_2P$/NF-P, NiO-FeO/NF-P, $Ni_2P$/NF-P and pure NF, respectively), the ECSA values are almost proportional with the physical surface area. Moreover, as the ECSA values are evaluated at the non-faradaic region, the ECSA values are mainly corresponded to the accessible physical surface area.

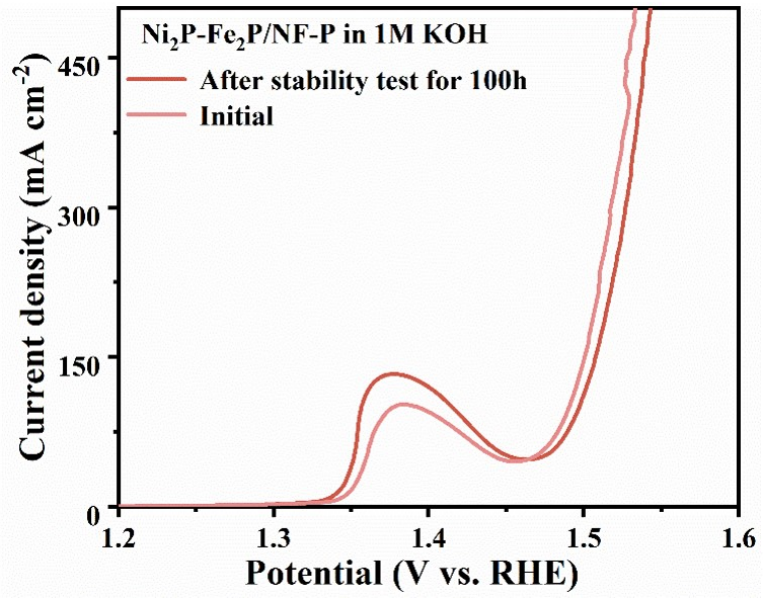


**Fig. S12.** LSV curves of $Ni_2P$-$Fe_2P$/NF-P before/after 100 h stability test at 500 mA $cm^{-2}$ for OER.

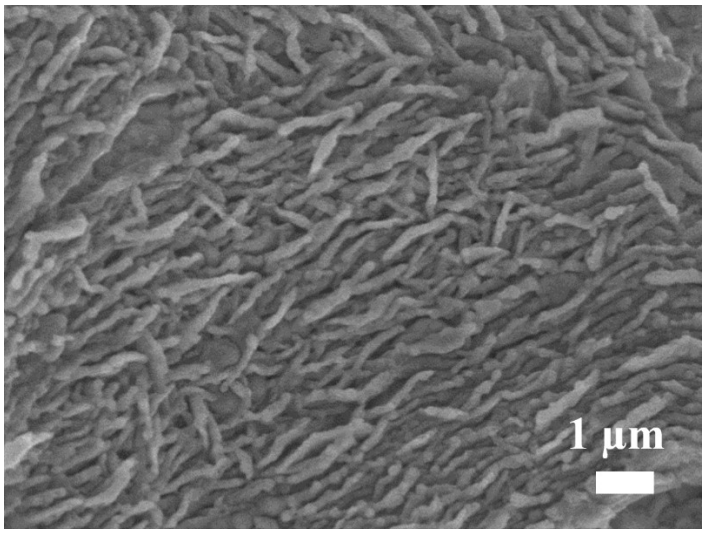


**Fig. S13.** SEM image of $Ni_2P$-$Fe_2P$/NF-P after stability test at 500 mA $cm^{-2}$ for OER.

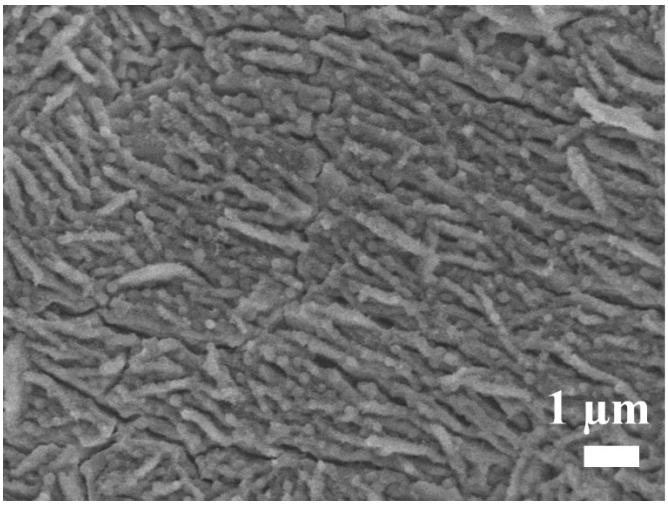


**Fig. S14.** SEM images of $Ni_2P$-$Fe_2P$/NF-P after stability test at 500 mA $cm^{-2}$ for UOR.

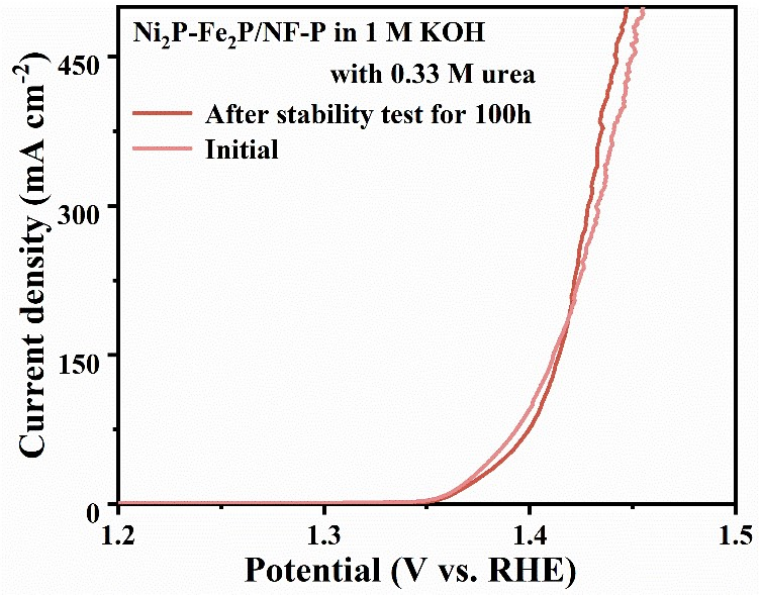


**Fig. S15.** LSV curves of $Ni_2P$-$Fe_2P$/NF-P before/after stability test at 500 mA $cm^{-2}$ for UOR.

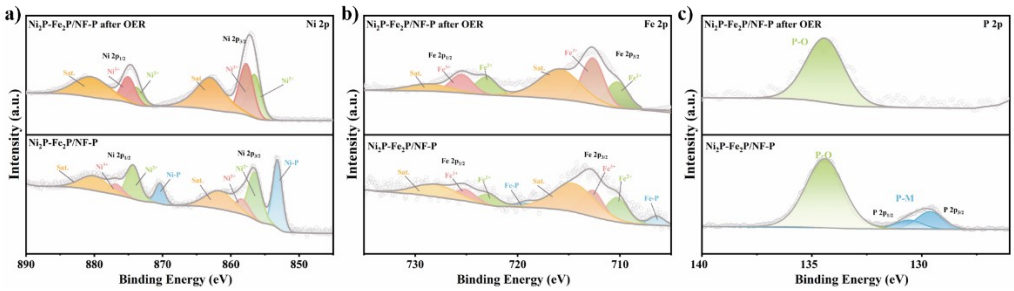


**Fig. S16.** XPS (a) Ni 2p, (b) Fe 2p and (f) P 2p spectra of $Ni_2P$-$Fe_2P$/NF-P before/after OER test.

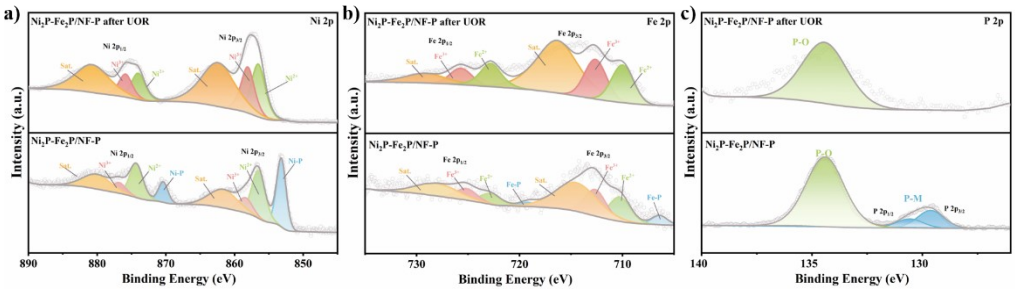


**Fig. S17.** XPS (a) Ni 2p, (b) Fe 2p and (f) P 2p spectra of $Ni_2P$-$Fe_2P$/NF-P before/after UOR test.

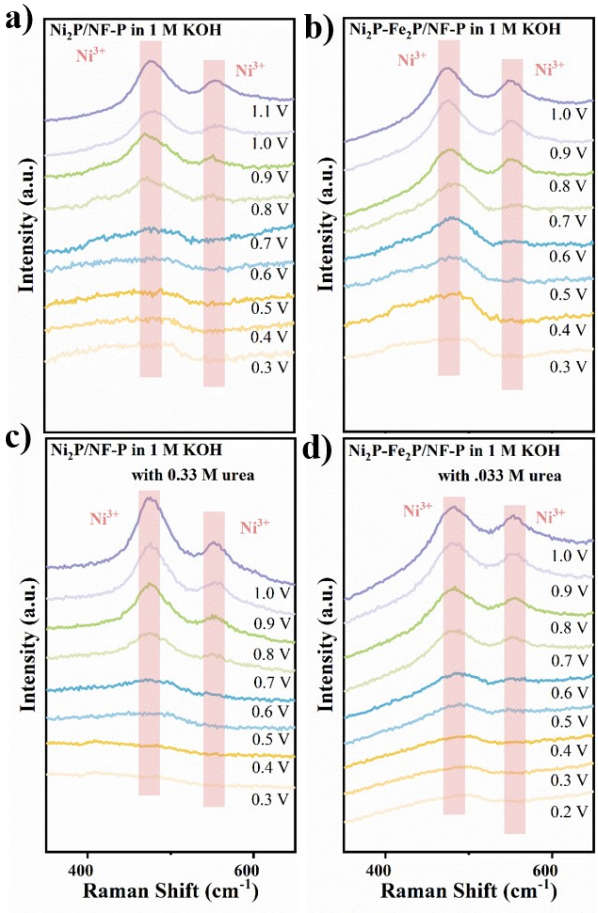


**Fig. S18.** In situ Raman spectra of (a, c) $Ni_2P$/NF-P and (b, d) $Ni_2P$-$Fe_2P$/NF-P during OER and UOR under various potentials (vs. Ag/AgCl), respectively.

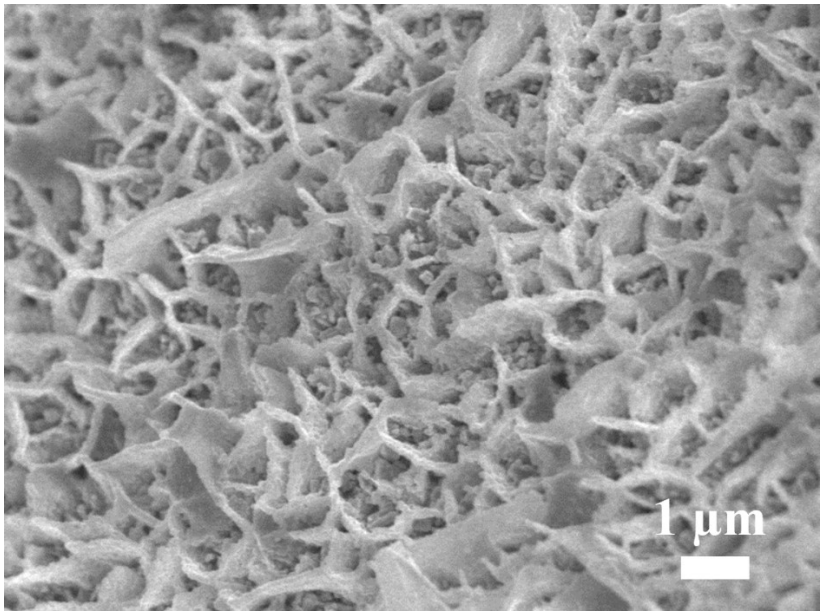


**Fig. S19.** SEM images of $Ni_2P$-$Fe_2P$/NF-D.

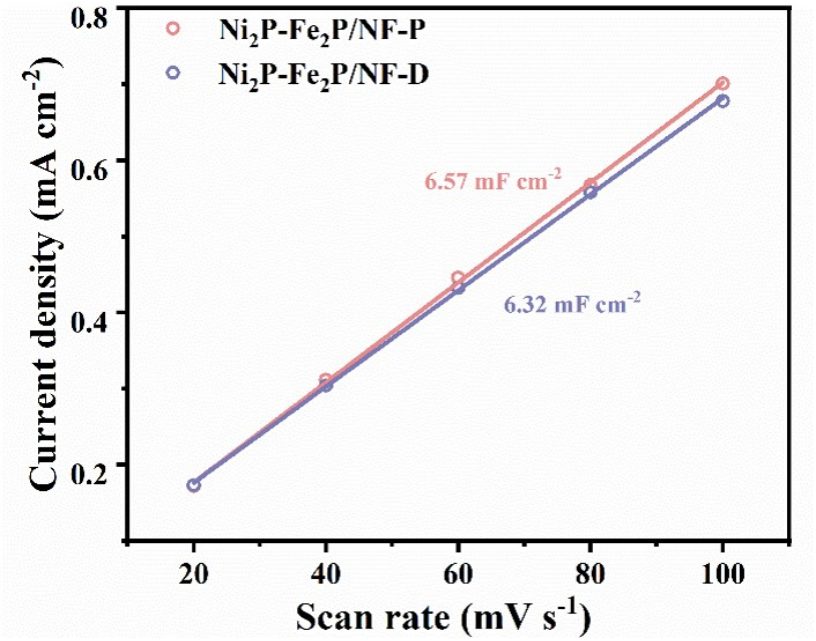


**Fig. S20.** $C_{dl}$ values of the comparison of electrocatalytic OER Performance between $Ni_2P$-$Fe_2P$/NF-P and $Ni_2P$-$Fe_2P$/NF-D.

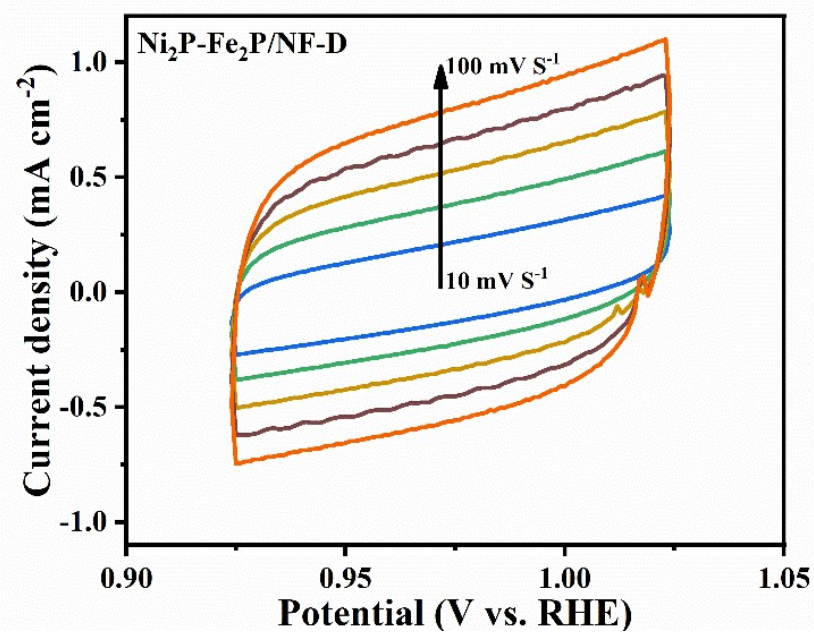


**Fig. S21.** CV curves of $Ni_2P$-$Fe_2P$/NF-D.

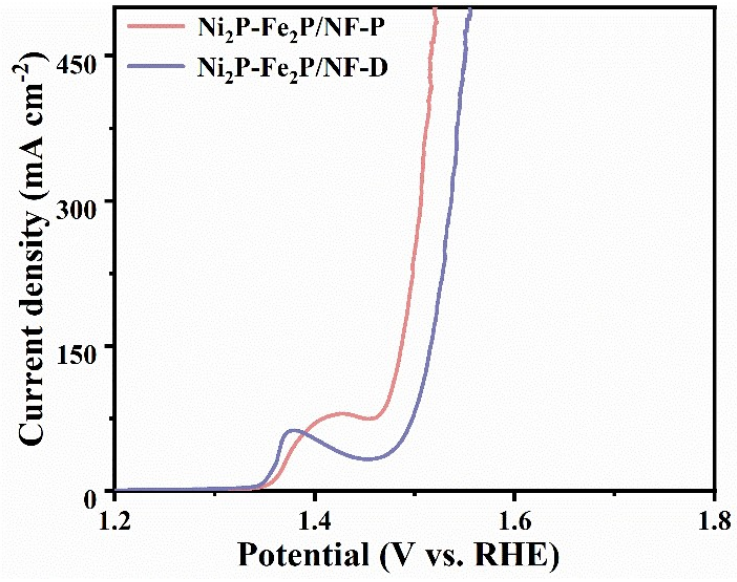


**Fig. S22.** LSV curves of the comparison of electrocatalytic OER Performance between $Ni_2P$-$Fe_2P$/NF-P and $Ni_2P$-$Fe_2P$/NF-D.

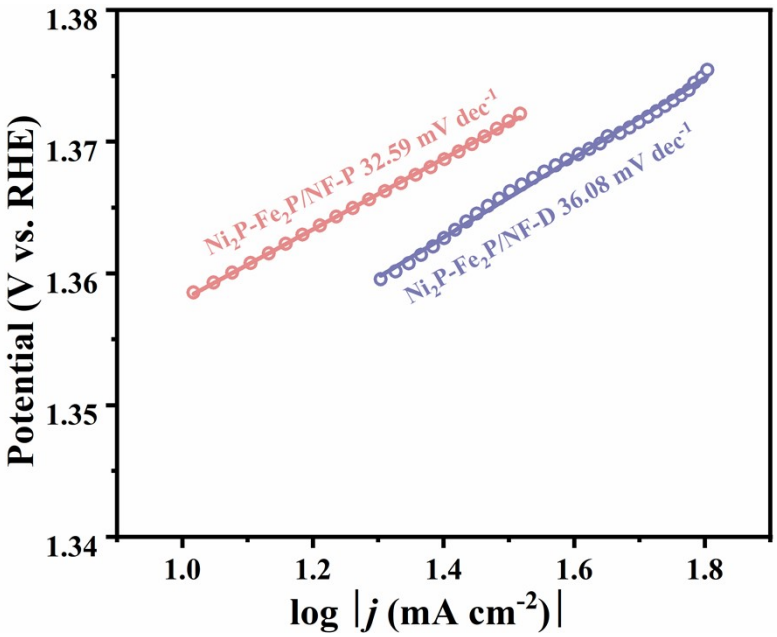


**Fig. S23.** Tafel plots of the comparison of electrocatalytic OER Performance between $Ni_2P$-$Fe_2P$/NF-P and $Ni_2P$-$Fe_2P$/NF-D.

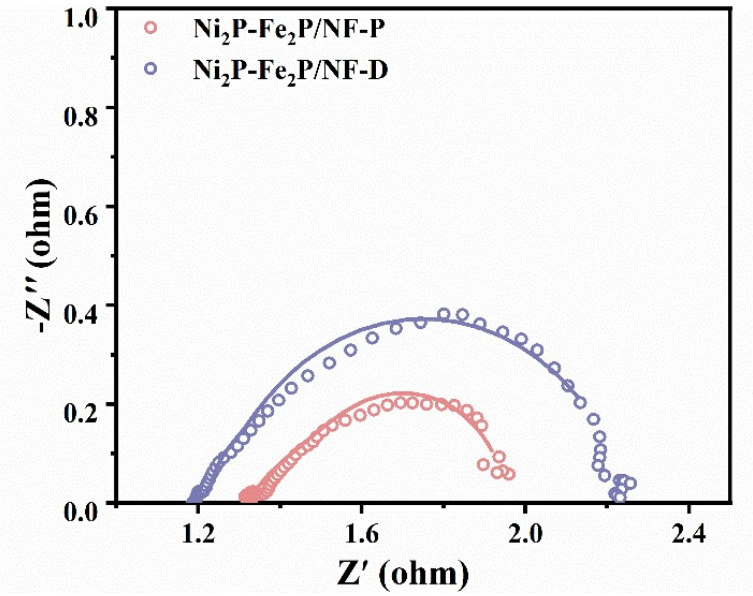


**Fig. S24.** EIS plots of the comparison of electrocatalytic OER Performance between $Ni_2P$-$Fe_2P$/NF-P and $Ni_2P$-$Fe_2P$/NF-D.

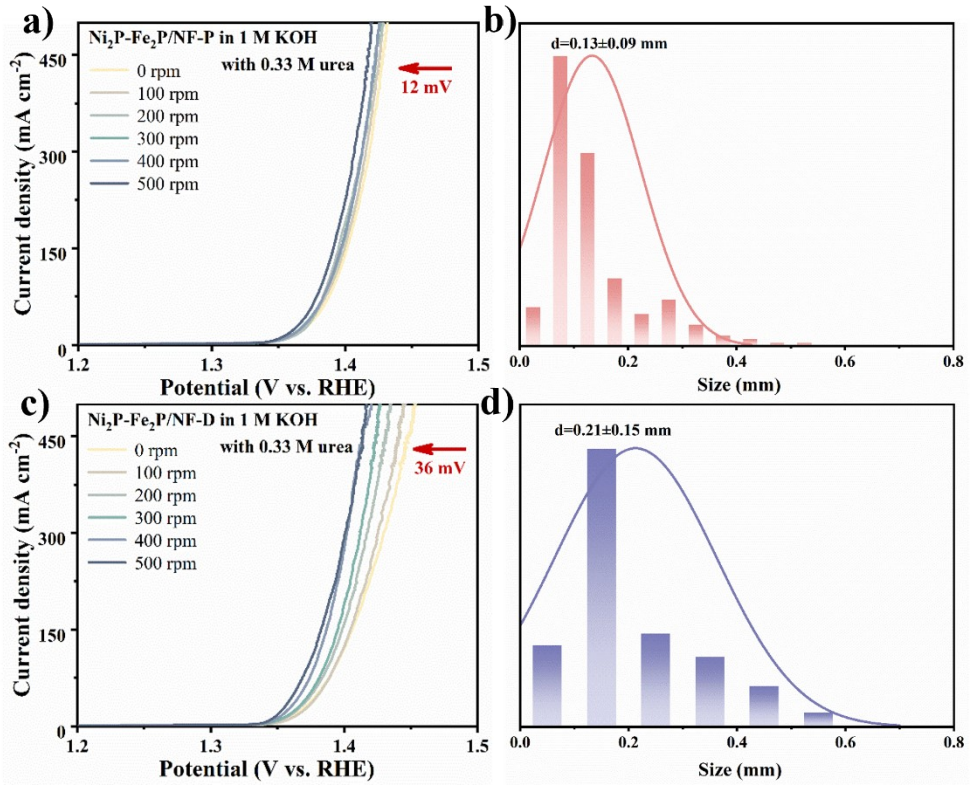


**Fig. S25.** LSV curves of (a) $Ni_2P$-$Fe_2P$/NF-P and (c) $Ni_2P$-$Fe_2P$/NF-D acquired at different stirring speeds in 1 M KOH with 0.33 M urea; The corresponding size distribution statistics for bubbles of (b) $Ni_2P$-$Fe_2P$/NF-P (d) $Ni_2P$-$Fe_2P$/NF-D.

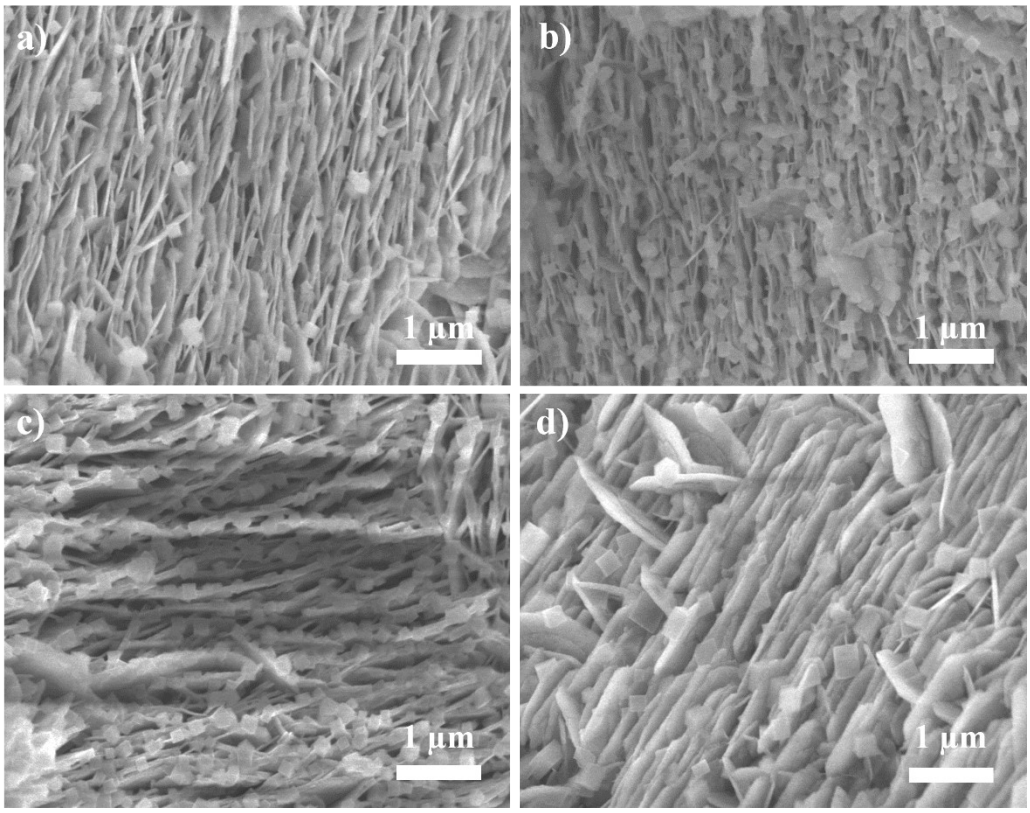


**Fig. S26.** SEM images of NiCo PBA/NF-P prepared by immersion in potassium cobalticyanide solutions of different concentrations: (a) 10 mg/mL, (b) 20 mg/mL, (c) 30 mg/mL, (d) 40 mg/mL

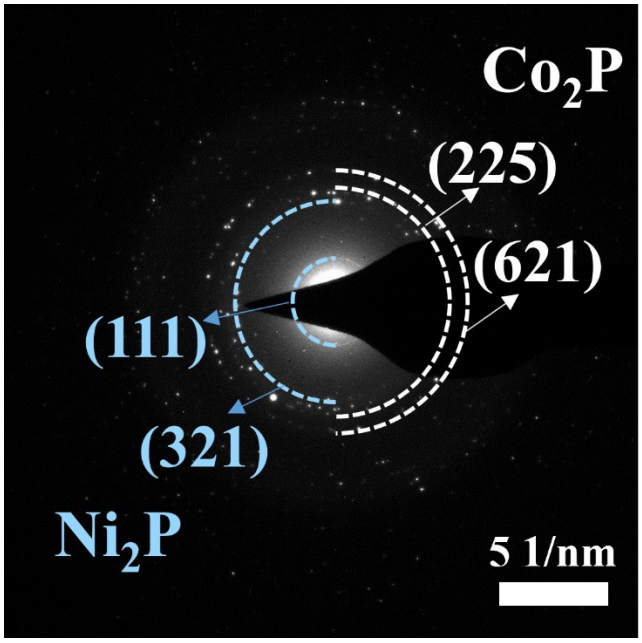


**Fig. S27.** SAED pattern of the $Ni_2P$-$Co_2P$/NF-P.

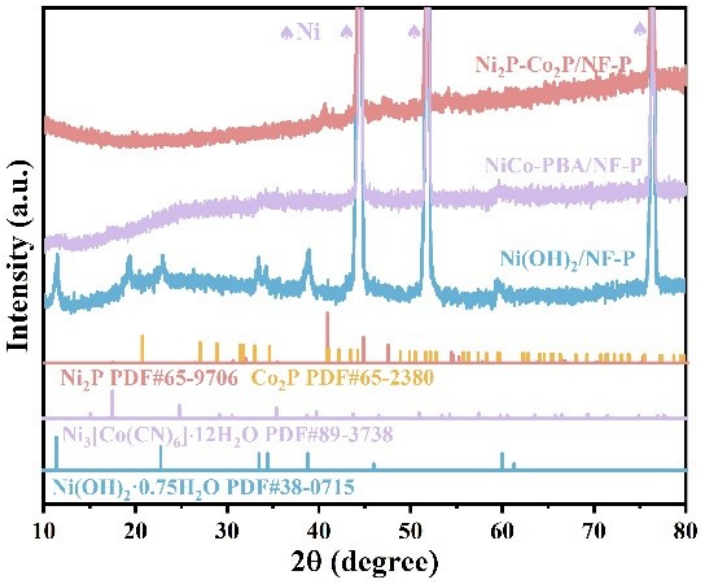


**Fig. S28.** XRD patterns of $Ni(OH)_2$/NF-P, NiCo PBA/NF-P and $Ni_2P$-$Co_2P$/NF-P.

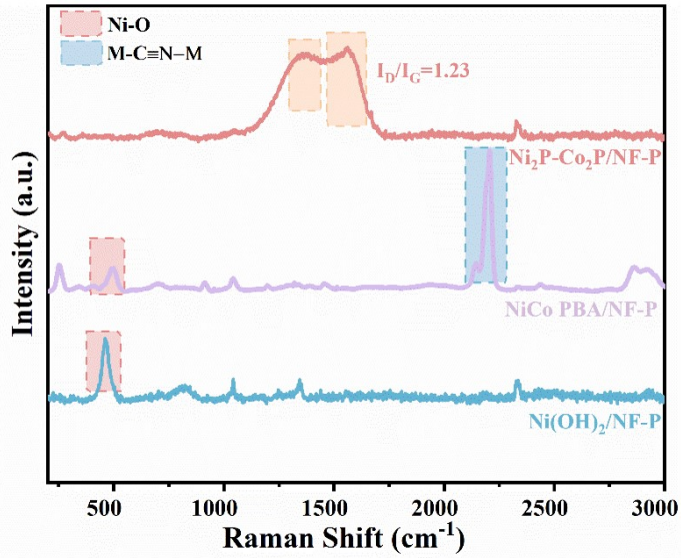


**Fig. S29.** Raman spectra of various samples.

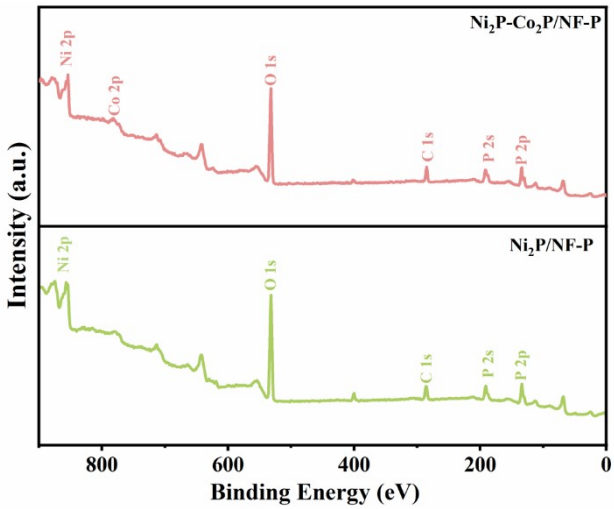


**Fig. S30.** XPS full survey of $Ni_2P$-$Co_2P$/NF-P and $Ni_2P$/NF-P.

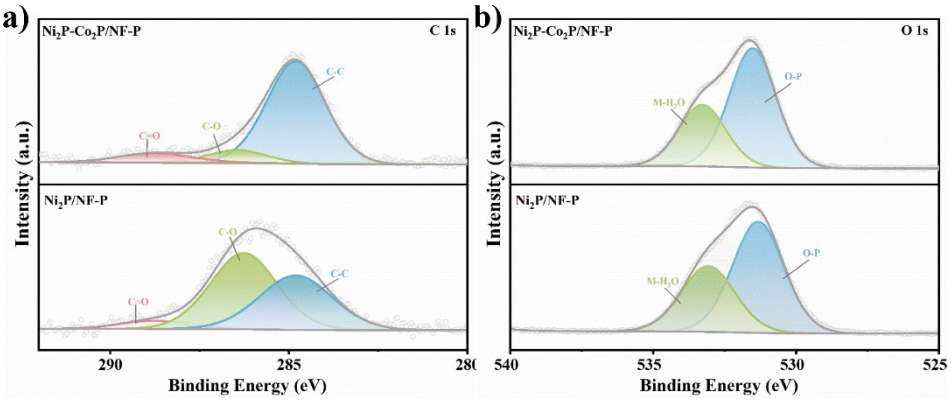


**Fig. S31.** XPS (a) C 1s; (b) O 1s spectrum of $Ni_2P$-$Co_2P$/NF-P and $Ni_2P$/NF-P.

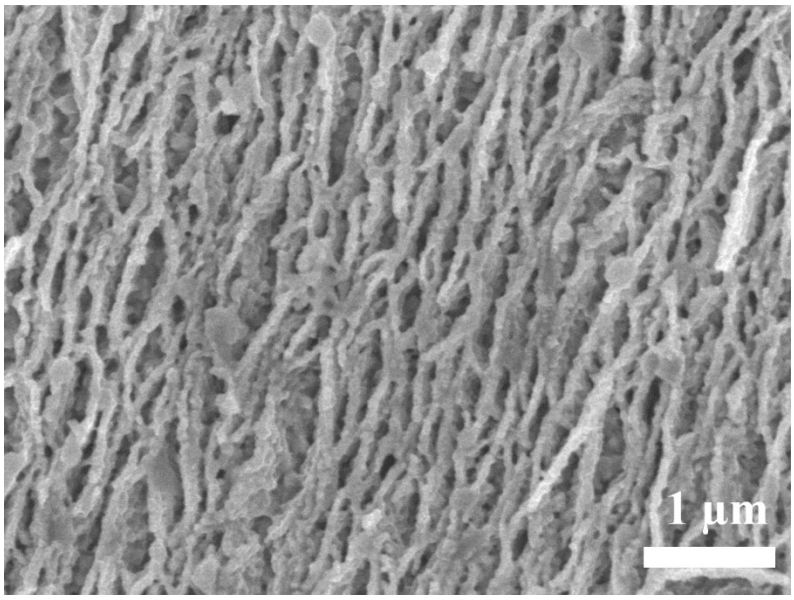


**Fig. S32.** SEM image of $Ni_2P$-$Co_2P$/NF-P after stability test at 500 mA $cm^{-2}$ for HER.

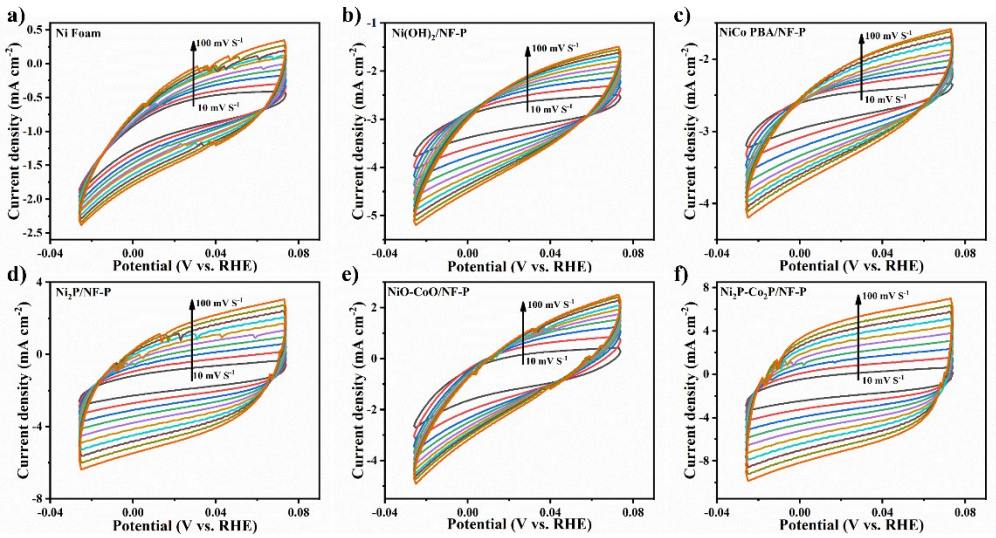


**Fig. S33.** CV curves of the as-prepared materials.

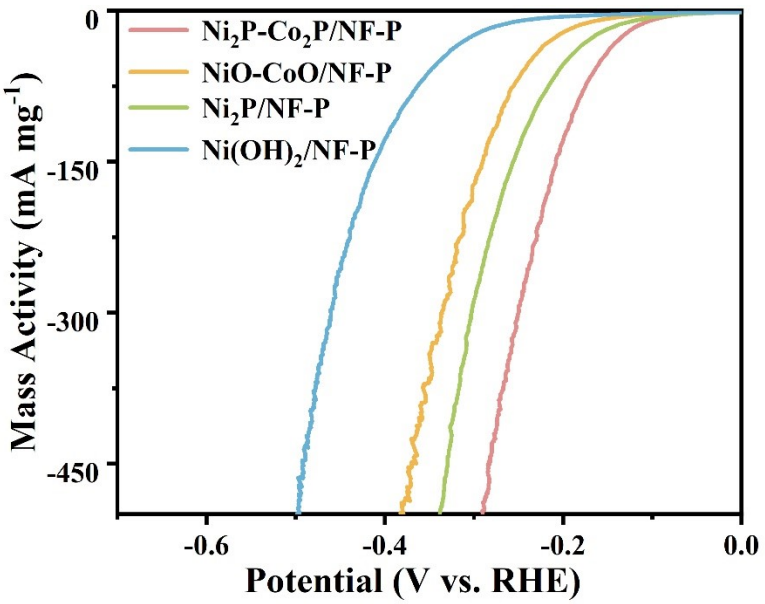


**Fig. S34** Active material loading mass-normalized LSV curves for HER corresponding to **Fig. 7a**.

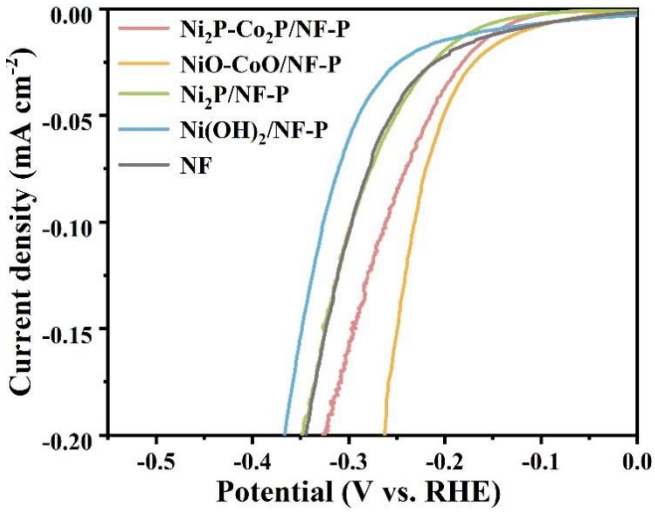


**Fig. S35.** ECSA-normalized LSV curves for HER corresponding to **Fig. 7a.**

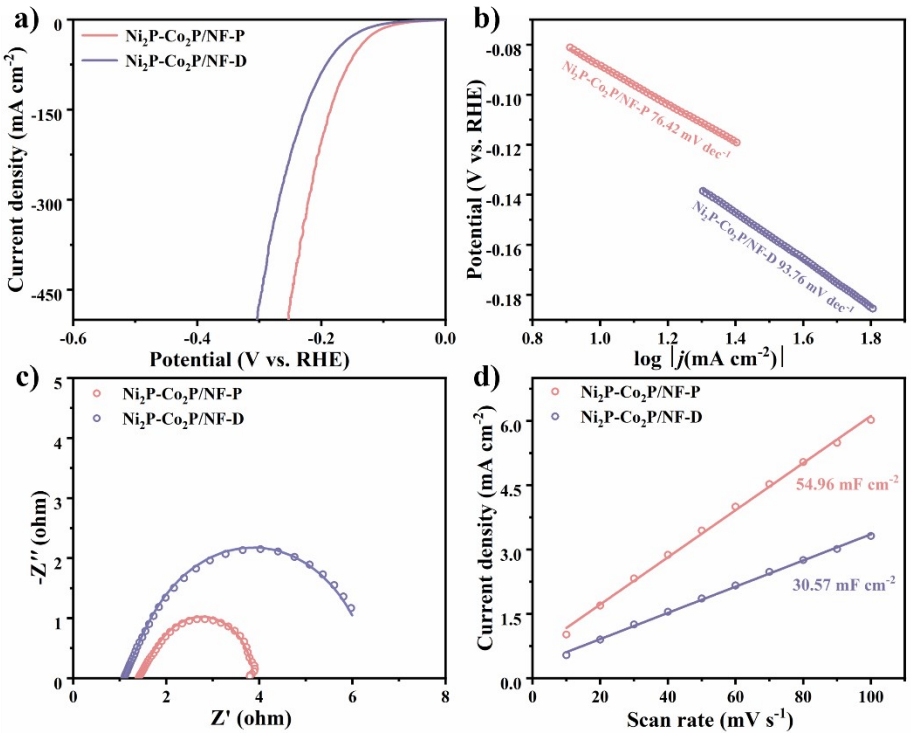


**Fig. S36.** (a) LSV curves, (b) Tafel plots, (c) EIS plots, (d) corresponding $C_{dl}$ values of the comparison of electrocatalytic HER Performance between $Ni_2P$-$Co_2P$/NF-P and $Ni_2P$-$Co_2P$/NF-D.

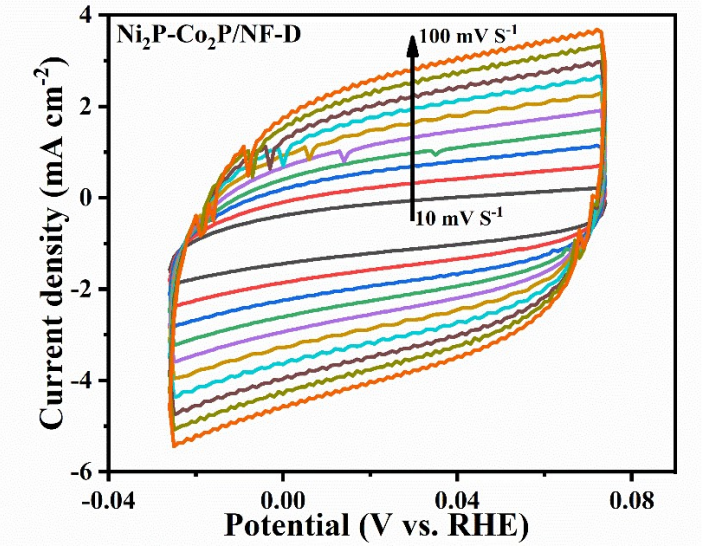


**Fig. S37.** CV curves of $Ni_2P$-$Co_2P$/NF-D.

## Supporting Tables

**Table S1.** Fitting values of EIS plots corresponding to **Fig. 3f**.

| | **NF** | **$Ni(OH)_2$/NF-P** | **NiFe PBA/NF-P** | **$Ni_2P$/NF-P** | **NiO-FeO/NF-P** | **$Ni_2P$-$Fe_2P$/NF-P** |
|---|---|---|---|---|---|---|
| | **(Ω)** | **(Ω)** | **(Ω)** | **(Ω)** | **(Ω)** | **(Ω)** |
| $R_s$ | 1.83 | 1.68 | 1.93 | 1.51 | 1.36 | 1.32 |
| $R_p$ | 12.73 | 0.09 | 1.66 | 7.01 | 0.34 | 0.02 |
| $R_{ct}$ | 47.03 | 2.23 | 8.53 | 11.13 | 1.68 | 0.39 |

**Table S2.** Fitting values of EIS plots corresponding to **Fig. S17**.

| | **$Ni_2P$-$Fe_2P$/NF-D (Ω)** |
|---|---|
| $R_s$ | 1.22 |
| $R_p$ | 0.02 |
| $R_{ct}$ | 1.0 |

**Table S3.** Fitting values of EIS plots corresponding to **Fig. 7d**.

| | **NF** | **$Ni(OH)_2$/NF-P** | **NiCo PBA/NF-P** | **$Ni_2P$/NF-P** | **NiO-CoO/NF-P** | **$Ni_2P$-$Co_2P$/NF-P** |
|---|---|---|---|---|---|---|
| | **(Ω)** | **(Ω)** | **(Ω)** | **(Ω)** | **(Ω)** | **(Ω)** |
| $R_s$ | 1.69 | 1.47 | 1.41 | 1.54 | 1.54 | 1.41 |
| $R_p$ | 12.97 | 5.06 | 7.99 | 0.53 | 1.23 | 0.49 |
| $R_{ct}$ | 43.75 | 67.9 | 57.37 | 5.36 | 11.08 | 1.97 |

**Table S4.** Active material loading mass of the as-prepared electrocatalysts.

| **Electrode materials** | **Catalyst loading (mg $cm^{-2}$)** |
|---|---|
| $Ni(OH)_2$/NF-P | 1.63 |
| NiFe PBA/NF-P | 1.8 |
| NiO-FeO/NF-P | 1.58 |
| $Ni_2P$-$Fe_2P$/NF-P | 1.61 |
| $Ni_2P$/NF-P | 1.03 |
| NiCo PBA/NF-P | 1.75 |
| NiO-CoO/NF-P | 1.56 |
| $Ni_2P$-$Co_2P$/NF-P | 1.58 |

**Table S5.** Comparison of the OER parameters of the $Ni_2P$-$Fe_2P$/NF-P with NiFe-based or pillar-parallel structured electrocatalysts at various current densities in 1 M KOH electrolyte.

| Electrode materials | Overpotential (mV) @j (mA $cm^{-2}$) | Tafel slope (mV $dec^{-1}$) | Stability j (mA $cm^{-2}$)@t (h) | Reference |
|---|---|---|---|---|
| **$Ni_2P$-$Fe_2P$/NF-P** | **226@20<br>246@100<br>290@500** | **32.59** | **500@100** | **This work** |
| p-$Co_9S_8$/NC/CF | 276@10<br>398@100 | 75 | - | [1] |
| NiCoP cage | 255@10<br>290@100 | 44.5 | 10@100 | [2] |
| $Ni(OH)_2$ PNAs | 206@10 | - | 1000@50 | [3] |
| NiFe NNG | 292@10 | 48 | 50@5.5 | [4] |
| P-$CoO_X$/NiFe LDHs | 220@10 | 38.7 | 100@500 | [5] |
| $R_{60}$-NiFe-LDH/NF | 298@500 | 39.5 | 500@1500 | [6] |
| $(Ni_{0.83}Fe_{0.17})_2P$/NF | 215@10<br>247@50 | 31.84 | 10@20 | [7] |
| Ru/NiFe-LDH/CuO | 211@10<br>300@500 | 48 | 500@500 | [8] |
| p-NiFeMo/NF | 274@100 | 57.1 | 500@72 | [9] |
| GD-NiFe LDH/S | 234@10<br>270@100 | 35.5 | 100@100 | [10] |

**Table S6.** Comparison of the UOR parameters of the $Ni_2P$-$Fe_2P$/NF-P with NiFe-based or pillar-parallel structured electrocatalysts at various current densities in 1 M KOH with 0.33 M urea electrolyte.

| Electrode materials | Potential (V) @j (mA $cm^{-2}$) | Tafel slope (mV $dec^{-1}$) | Stability j (mA $cm^{-2}$)@t (h) | Reference |
|---|---|---|---|---|
| **$Ni_2P$-$Fe_2P$/NF-P** | **1.35@20<br>1.37@100<br>1.40@500** | **21.55** | **500@100** | **This work** |
| A-NiFeV/NF | 1.33@20<br>1.39@100 | - | 100@50 | [11] |
| NiFeSbP/GB | 1.50@100 | - | 100@20 | [12] |
| O-NFF | 1.409@100<br>1.47@500 | 12.1 | 100@12 | [13] |
| $NiFeCoS_x$@$FeNi_3$ | 1.42@10 | 97 | 100@2 | [14] |
| Ag@NiFe-LDH/$NiFe_2O_4$ | 1.389@50 | - | 10@25 | [15] |
| NiFe LDH-$Ni_3S_2$ | 1.34@10 | 24 | - | [16] |
| NiHCF/NF | 1.39@100 | 16 | 100@100 | [17] |

**Table S7.** Comparison of the HER parameters of the $Ni_2P$-$Co_2P$/NF-P with NiCo-based or pillar-parallel structured electrocatalysts at various current densities in 1 M KOH electrolyte.

| Electrode materials | Overpotential (mV) @j (mA $cm^{-2}$) | Tafel slope (mV $dec^{-1}$) | Stability j (mA $cm^{-2}$)@t (h) | Reference |
|---|---|---|---|---|
| **$Ni_2P$-$Co_2P$/NF-P** | **112@20<br>168@100** | **76.42** | **500@100** | **This work** |
| p-$Co_9S_8$/NC/CF | 540@100 | 92 | - | [1] |
| Fe-Co-O/Co@NC-mNS/NF | 112@10<br>201@100 | 96 | 10@50 | [18] |
| $Ce_{0.10}$-NiCoP | 96@10<br>166@10<br>192@100 | 94.75 | 20@100 | [19] |
| $Ni_2P$/(Co,Ni)OOH/NF | 169@100 | 123 | 10@36 | [20] |
| (NiFe/NiCo)S@NF | 185@10 | 76 | 10@12 | [21] |
| $NiCo_2O_4$@$NiCo(OH)_2$ | 121@10<br>306@100<br>691@500 | 83.2 | 200@100 | [22] |
| $NiCo_{(nf)}$-P | 199@100 | 112 | 1000@30 | [23] |
| CoP@CoP@$(Co/Ni)_2P$ | 147@10 | 68.06 | 10@30 | [24] |

**Table S8.** Comparison of the overall water splitting parameters of $Ni_2P$-$Fe_2P$/NF-P || $Ni_2P$-$Co_2P$/NF-P electrocatalysts at various current densities in 1 M KOH electrolyte.

| Electrode materials | potential (V) @ j (mA $cm^{-2}$) | Stability j (mA $cm^{-2}$)@t (h) | Reference |
|---|---|---|---|
| **$Ni_2P$-$Fe_2P$/NF-P \|\| $Ni_2P$-$Co_2P$/NF-P** | **1.557@20<br>1.77@100<br>2.234@500** | **500@100** | **This work** |
| $NiFeCoS_x$@$FeNi_3$ \|\| $NiFeCoS_x$@$FeNi_3$ | 1.54@10<br>1.80@100 | - | [14] |
| Ni-1T-$MoS_2$ \|\| Ni-1T-$MoS_2$ | 1.54@10<br>1.82@50 | - | [25] |
| Nb–$Co_4N$/NF \|\| Nb–$Co_4N$/NF | 1.61@10<br>1.68@20 | 200@10 | [26] |
| NiCoFe-LDH \|\| NiCoFe-LDH | 1.56@10 | 100@18 | [27] |
| CoFe-P/NF \|\| CoFe-P/NF | 1.58@10<br>1.80@50 | 100@40 | [28] |
| CoFe@NiFe-200/NF \|\| CoFe@NiFe-200/NF | 1.59@10<br>1.77@100 | 10@24 | [29] |
| $B_{10}$–FeCoNi-LDH@NF \|\| $B_{10}$–FeCoNi-LDH@NF | 1.547@10<br>1.83@50 | 100@100 | [30] |
| NiFeP-CNT@NiCo/CP \|\| NiCoP-CNT@NiCo/CP | 1.58@10 | 10@100 | [31] |

**References**

1. Y. Zhao, T. Li, Q. Wang, Y. Ai, R. Hou, A. Habib, G. Shao, F. Wang and P. Zhang, Journal of Materials Chemistry A, 2024, 12, 23872-23879.

2. Y. Zhou, Y. Hu, S. Lu, D. Wang, D. Ma, X. Gong and Q. Yue, Advanced Functional Materials, 2024, 34, 2401195.

3. J. Kang, G. Liu, Q. Hu, Y. Huang, L.-M. Liu, L. Dong, G. Teobaldi and L. Guo, Journal of the American Chemical Society, 2023, 145, 25143-25149.

4. Z. Lyu, S. Yu, M. Wang, P. Tieu, J. Zhou, Q. Shi, D. Du, Z. Feng, X. Pan, H. Lin, S. Ding, Q. Zhang and Y. Lin, Small, 2024, 20, 2308278.

5. H.-M. Xu, C.-J. Huang, H.-R. Zhu, Z.-J. Zhang, T.-Y. Shuai, Q.-N. Zhan, V. Y. Fominski and G.-R. Li, Small, 2024, 20, 2400201.

6. B. Wang, J. Chen, L. Luo, G. Huang, Q. Shi, Q. Wei, M. Shang and Q. Liu, Advanced Functional Materials, 2025, 35, 2505763.

7. Z. Wang, S. Liu, J. Du, Y. Xing, Y. Hu, Y. Ma, X. Lu and C. Wang, Green Chemistry, 2024, 26, 7779-7788.

8. Y. Yang, H. Gao, C. Zhu, W. Sun, J. Zeng, X. Wang and X. Tian, Advanced Functional Materials, 2025, n/a, e14599.

9. Y. Wei, L. Yi, R. Wang, J. Li, D. Li, T. Li, W. Sun and W. Hu, Small, 2023, 19, 2301267.

10. J. Zhang, Q. Chen, P. Zhao, A. Cai, X. Fan, W. Peng and Y. Li, Small, 2025, 21, 2409265.

11. H. Yang, L. Ge, J. Guan, B. Ouyang, H. Li and Y. Deng, Journal of Colloid and Interface Science, 2024, 653, 721-729.

12. H. Shooshtari Gugtapeh and M. Rezaei, ACS Applied Energy Materials, 2022, 5, 15689-15700.

13. J. Kim, M.-C. Kim, S. S. Han and K. Cho, Advanced Functional Materials, 2024, 34, 2315625.

14. J. Shen, Q. Li, W. Zhang, Z. Cai, L. Cui, X. Liu and J. Liu, Journal of Materials Chemistry A, 2022, 10, 5442-5451.

15. X. Zhang, J. Zhang, Z. Ma, L. Wang, K. Yu, Z. Wang, J. Wang and B. Zhao,

Journal of Colloid and Interface Science, 2024, 665, 313-322.

16. Z.-H. Zhang, Z.-R. Yu, Y. Zhang, A. Barras, A. Addad, P. Roussel, L.-C. Tang, M. Naushad, S. Szunerits and R. Boukherroub, Journal of Materials Chemistry A, 2023, 11, 19578-19590.

17. G. Kalaiyarasan, D. Lee, J. W. Lee and M. J. Ko, ACS Applied Materials & Interfaces, 2024, 16, 69142-69152.

18. T. I. Singh, G. Rajeshkhanna, U. N. Pan, T. Kshetri, H. Lin, N. H. Kim and J. H. Lee, Small, 2021, 17, 2101312.

19. M. Zhang, H. Xu, H. Yang, X. Shang, M. Yuan, Y. Fu, Y. Xiao, S. Wang, X. Wang, B. Jia, S. Li and T. Ma, Small, 2025, 21, 2504837.

20. L. Zhang, Z. Wang, J. Zhang, Z. Lin, Q. Zhang, W. Zhong and G. Wu, Nano Research, 2023, 16, 6552-6559.

21. L. Fathyunes, C. Muilwijk and D. Brabazon, International Journal of Hydrogen Energy, 2024, 78, 622-633.

22. G. Chen, D. Chen, J. Huang, C. Zhang, W. Chen, T. Li, B. Huang, T. Shao, J. Li and K. K. Ostrikov, ACS Applied Materials & Interfaces, 2021, 13, 45566-45577.

23. Z. Xu, C.-L. Yeh, J.-L. Chen, J. T. Lin, K.-C. Ho and R. Y.-Y. Lin, ACS Sustainable Chemistry & Engineering, 2022, 10, 11577-11586.

24. H. Zhang, Y. Q. Wu, X. D. Wang, C. P. Li, Z. Y. Xiao, Y. R. Liu, Y. Deng, Z. J. Li and L. Wang, Chemical Engineering Journal, 2023, 463.

25. G. Wang, G. Zhang, X. Ke, X. Chen, X. Chen, Y. Wang, G. Huang, J. Dong, S. Chu and M. Sui, Small, 2022, 18, 2107238.

26. X. H. Chen, Q. Zhang, L. L. Wu, L. Shen, H. C. Fu, J. Luo, X. L. Li, J. L. Lei, H. Q. Luo and N. B. Li, Materials Today Physics, 2020, 15, 100268.

27. Y. Zhuang, S. Meng, Y. Wu, J. Li, X. Yang, C. Yuan, T. Peng and D. Guo, Journal of Colloid and Interface Science, 2025, 700, 138645.

28. D. Duan, D. Guo, J. Gao, S. Liu and Y. Wang, Journal of Colloid and Interface Science, 2022, 622, 250-260.

29. R. Yang, Y. Zhou, Y. Xing, D. Li, D. Jiang, M. Chen, W. Shi and S. Yuan, Applied Catalysis B: Environmental, 2019, 253, 131-139.

30. L. Ma, X. Li, G. Zhang, Y. Zhang, H. Dong, J. Liao, R. Han and L. Zhang, International Journal of Hydrogen Energy, 2025, 124, 251-262.
31. Z. Wang, C. Wei, X. Zhu, X. Wang, J. He and Y. Zhao, Journal of Materials Chemistry A, 2021, 9, 1150-1158.